

Creation of super-high-flux photo-neutrons and gamma-rays > 8 MeV using a petawatt laser to irradiate high-Z solid targets

E.Liang¹, W.Lo², B.Cage¹, E.Fang¹, S.Arora¹, K.Q.Zheng¹, H.Quvedo², S.A.Bruce², M. Spinks², E. Medina², A. Helal², T. Ditmire²

1 Rice University, Houston, TX 77005

2 University of Texas at Austin, Austin, TX 78712

Abstract

We report the creation of super-high-flux gamma-rays with energy >8 MeV and photo-neutrons via the (γ ,n) reaction near giant dipole resonance energies (8 - 20 MeV), using the ~130 J Texas Petawatt laser to irradiate high-Z (Au, Pt, Re, W) targets of mm - cm thickness, at laser intensities up to $\sim 5 \times 10^{21}$ W/cm². We detected up to \sim several $\times 10^{12}$ gamma-rays > 8 MeV ($\sim 3\%$ of incident laser energy) and $\sim 10^{10}$ photo-neutrons per shot. Due to the short pulse and narrow gamma-ray cone ($\sim 17^\circ$ half-width) around laser forward, the peak emergent gamma-ray flux >8 MeV reached $\sim 10^{27}$ gammas/cm²/sec, and the peak emergent neutron flux reached $\sim 10^{20}$ neutrons/cm²/sec. Such intense gamma-ray and neutron fluxes are among the highest achieved for short-pulse laser experiments. They will facilitate the study of nuclear reactions requiring super-high-flux of gamma-rays or neutrons, such as the creation of r-process elements. These results may also have far-reaching applications for nuclear energy, such as the transmutation of nuclear waste.

1. INTRODUCTION

Modern ultra-intense short-pulse lasers are efficient accelerators of relativistic electrons (Gibbon 2005). When these relativistic electrons interact with high-Z solid targets, they produce copious amounts of gamma-rays, which in turn create electron-positron pairs (Liang et al 1998, Chen H. et al 2009, Liang et al 2015) and photo-neutrons via (γ,n) reactions (Makwana et al 2017). While many different acceleration mechanisms have been proposed for the relativistic “hot” electrons (Gibbon 2005, Levy et al 2014), it is generally assumed that the gamma-rays are mainly emitted by electron bremsstrahlung against target ions (Rybicki & Lightman 1979, Chen et al 2009, Henderson et al 2014). The bremsstrahlung spectrum falls exponentially with photon energy, with the exponential constant determined by the average energy of primary hot electrons and secondary electrons and positrons (Henderson 2015). The bremsstrahlung emission from laser-solid interactions has been well characterized below ~ 6 MeV as an exponential by many groups using filter-stack spectrometers (FSS. Chen et al 2009, Henderson 2015). However, the FSS cannot determine the gamma-ray spectrum > 6 MeV (Liang et al 2022). While other schemes (e.g. nuclear activation thresholds (Leeman et al 2001), forward Compton scattering (Morgan et al 1991, Kojima et al 2014)) have been used in some laser experiments, they are strongly model-dependent. Most laser-created gamma-ray spectra > 6 MeV are based on few-channel forward-folding using a simple exponential model (Belm et al 2018, Gunther et al 2022).

A radically new type of high-resolution gamma-ray spectrometer called scintillation attenuation spectrometer (SAS) was recently developed by our group in collaboration with MD Anderson Cancer Center medical imaging group, based on 2D imaging of scintillation light from a highly pixelated LYSO crystal matrix with mm-sized pixels (Liang et al 2022). The SAS can measure gamma-ray spectrum from 0.25 MeV - 50 MeV with 0.5 MeV resolution. From 2016-2018, we obtained ~ 180 gamma-ray spectra from two SAS viewing different angles, from mm-cm thick Au and Pt targets irradiated by the ~ 130 J Texas Petawatt laser (TPW) in Austin Texas, at intensities $\sim 10^{21}$ W.cm². However, a robust inversion algorithm to extract model-independent gamma-ray spectra from SAS images was only completed, calibrated and validated in 2021 (Liang et al 2022). In 2022 we began systematic extraction of TPW gamma-ray spectra from archived SAS data. One unexpected discovery was the presence of a broad high-energy (> 8 MeV) bump-like feature sitting on top of the conventional exponential bremsstrahlung spectrum (Fig.1). This broad feature peaks at ~ 13 -20 MeV and often contains more energy than the bremsstrahlung component. However, this high-energy excess > 8 MeV is absent in spectra obtained at angles far from laser forward (LF), where only the exponential bremsstrahlung spectrum is observed (Liang et al 2022) For easy reference, hereafter we refer to the broad high-energy bump-like excess as HEB, and the low-energy bremsstrahlung component as LEB. Fig.1 shows two SAS raw images and their corresponding gamma-ray spectra obtained using the inversion algorithm published in (Liang et al 2022). Fig1a shows the HEB and LEB components at LF, while Fig.1b shows only the LEB component at 90° from LF.

Coincidentally, the cross-section for (γ,n) photo-neutron reactions of high-Z elements exhibits a broad peak spanning 8 - 20 MeV, corresponding to the giant dipole resonance (GDR, Makwana et al 2017, Kimura et al 2016)(cf. Fig.2). The strong overlap of the GDR cross-section with the HEB gamma-ray excess of Fig.1 motivated new TPW experiments in 2022 to study photonuclear reactions in the GDR regime. The goal was two-fold. We wanted to use photo-neutron yields to independently characterize the gamma-ray spectrum > 8 MeV. At the same time, we wanted to explore using TPW as a platform to create high-flux photo-neutrons.

We completed 60 shots in 2022 with TPW irradiating mm - cm thick targets of Au, Pt, Re and W, with intensities up to $\sim 5 \times 10^{21} \text{ W.cm}^{-2}$. We achieved high-fluxes of photon-neutrons and gamma-rays $> 8 \text{ MeV}$. We detected up to several $\times 10^{12}$ gamma-rays $> 8 \text{ MeV}$ ($\sim 3\%$ of laser energy) and $\sim 10^{10}$ photo-neutrons per shot. The highest emergent gamma-ray flux $> 8 \text{ MeV}$ reached $\sim 10^{27} \text{ gammas/cm}^2/\text{sec}$, and the highest emergent photo-neutron flux reached $\sim 10^{20} \text{ neutrons/cm}^2/\text{sec}$, which exceeds the threshold for r-process element creation (Fig.3) (Kajimo et al 2019, Chen et al 2019, Tanaka et al 2020, Goriely & Pinedo 2015). The super-high gamma-ray flux should also facilitate the study of photo-fission reactions and fission products of actinides (Naik et al 2011, Pomme 1994).

2. EXPERIMENT SETUP AND DIAGNOSTICS

Fig.4 is a sketch of the TPW high-intensity target chamber (TC1, Martinez et al 2005) where all our experiments were carried out with sample placements of diagnostics. In 2022 we deployed one e+e- magnetic spectrometer (MS, 0.1-65 MeV) inside TC1, and two SAS's (0.25-50 MeV) outside the TC1 tank wall. A FSS ($\leq 6 \text{ MeV}$) is co-located with each SAS. Typically, one SAS will sit inside the gamma-ray cone ($\sim 17^\circ$ half-angle, Henderson et al 2014, Henderson 2015) near laser forward (LF), and a second SAS will be $\sim 90^\circ$ from LF. Up to 15 gamma dosimeters (0.02-6 MeV) were attached to the outside tank wall, replaced once a day, around the forward gamma-ray cone to monitor the gamma dose angular distribution. Neutron bubble detectors were attached to the outside tank wall at various positions to measure the neutron dose. The positions of the MS, SAS and FSS can be moved from shot to shot as we perform the angle sweep of the e+e- pair and gamma-ray outputs. Fig. 5 shows typical TPW focal spot intensity and time profiles during our run. Table 1 summarizes the laser and target parameters of our 2022 run. Except for a few outliers, TPW pulse energy and intensity were stable during our 60-shot run. But the pulse duration for the first half of our run was longer than usual, leading to an average pulse length of $\sim 160 \text{ fs}$ instead of the normal average of 140 fs .

During the second half of our run we employed a special technique to enhance the gamma-ray output. We discovered that by sending in a low-energy OPA prepulse to create a micro-divot of \sim Rayleigh length in size before sending in the main pulse, the gamma-ray output can be increased by up to a factor of 2. This technique was used in all our shots in which photo-neutron outputs were measured.

Two types of laser targets were studied in 2022: disks and capsules, with total thickness ranging from 1 mm to 2 cm. Flat circular or square disks of thickness from 1 mm to 1 cm of pure Au, Pt, Re and W were used to study the Z-dependence of gamma-rays and e+e- pairs. Neutrons were measured only for Pt disks. Fig.6 shows the typical geometry of a capsule target, which consists of a cm-square front cover made of pure Re (thickness 1.8 mm to 1cm) acting as the gamma-ray "converter", attached to a cm-cube of W "catcher" with a cylindrical divot along the central axis. The capsule design is for later experiments in which potentially activatable material can be securely housed and contained inside the divot while safely shielded from the target chamber and target handlers. In this paper we only report the results from empty capsules such that the gamma-rays and neutrons are produced only by the Re converter and W catcher. Data from filled capsules remain to be processed and analyzed. We chose Re as the converter material because Re target makes the smallest crater among the four elements, due to its low thermal conductivity, high density, high melting and boiling points, and high heats of fusion and vaporization. Hence Re targets allow the maximum number of laser shots within a given target area.

3. RESULTS

Fig.1 shows typical 2022 gamma-ray spectra obtained from our two SAS spectrometers. Near LF (Fig.1a) we obtain gamma-ray spectra containing a broad "bump" peaking around 13 - 20 MeV, in addition to the exponential component consistent with bremsstrahlung emission. We also use the dosimeter data to independently normalize the amplitude of the SAS spectra. The broad HEB feature is absent in the SAS data at $\sim 90^\circ$ from LF (Fig.1b), and we detect only the exponential component consistent with bremsstrahlung emission (LEB).

When the HEB excess > 8 MeV was first discovered in our 2016-2018 SAS data, we had no independent data to confirm or disprove it. Hence in our 2022 TPW experiment, we adopted two new approaches to independently constrain and ascertain the SAS gamma-ray spectrum. First, since the (γ, n) reaction cross-section has a well-characterized GDR peak spanning 8 MeV - 18 MeV for all high-Z elements (Fig.2), we can use the photo-neutron yield to independently constrain the gamma-ray spectrum in this energy range. Second, the high-energy e^+e^- pairs created by gamma-rays > 8 MeV are much less attenuated in thick targets than low-energy pairs created by bremsstrahlung gamma-rays < 6 MeV. By measuring the emergent spectra of electrons and positrons from cm-thick targets we should be able to cross-check the gamma-ray spectrum > 8 MeV which created them because pairs created by bremsstrahlung photons should peak at only 1-2 MeV. In particular, for cm-thick targets, we expect the electron and positron spectra to resemble each other since any sheath electric field would be negligible, and most of the laser accelerated primary hot electrons would be absorbed. It turns out this was indeed the case. Both the photo-neutron data and e^+e^- pair data for cm-thick targets are consistent with the gamma-ray spectrum of Fig.1a, and completely inconsistent with hot electron bremsstrahlung as the sole source of gamma-rays.

In most of our 2022 shots, the energy of the HEB gamma-rays > 8 MeV exceeds the energy of the LEB component < 8 MeV and reaches up to $\sim 3\%$ of incident laser energy. For example in Fig.1a, the energy ratio of HEB/LEB is > 5 . Without the HEB component, our photo-neutron yield would have been much lower. In fact our GEANT4 simulations show that the photo-neutron yield from pure hot electron bremsstrahlung gamma-rays would be ~ 30 times less than what is observed. We perform such GEANT4 simulations by using the observed hot electron spectrum (Fig.7) and iterate the hot electron injection number to achieve the observed MS data and dosimeter data for gamma-rays < 6 MeV. We also cross-calibrate the SAS spectrum such as Fig.1a using both photo-neutron yields (which constrain the HEB) and dosimeter data (which constrain the LEB amplitude). In general, the HEB/LEB ratio obtained from the two methods are consistent to within 20%. While this does not prove the detailed spectral shapes of either the HEB or the LEB, it serves to confirm the existence of the HEB component independent of the SAS spectrum.

On the other hand the electron and positron spectra of cm-thick targets do tightly constrain the spectral shape of the HEB, since the observed e^+e^- spectra faithfully represent the "birth" spectra of the pairs produced by HEB gamma-rays, with little sheath field effects or contamination from primary hot electrons. Fig.7 compares the emergent e^+e^- pair spectra for a cm-thick Pt target with two different GEANT4 simulations: (a) pure hot electrons injection with no additional HEB gamma-rays, (b) hot electron injection plus the HEB gamma-rays of Fig.1. We see that GEANT4 predictions for case (a) completely disagrees with observed e^+e^- MS data, while GEANT4 predictions for case (b) agrees well with observed MS data. It is important to note that the observed

electron and positron spectra are similar in both shape and number, proving that both are dominated by pairs.

Fig.8 compares the photo-neutron yield and spectra predicted by GEANT4 for a 4.5 mm thick Pt target of case (a) and (b) above. Once again the experimental data strongly disagrees with case (a) and agrees with case (b), with a measured isotropic neutron yield of $\sim 10^{10}$ neutrons.

In summary, by combining the e+e- spectral data for cm-thick targets and photo-neutron yields, we convincingly prove that the gamma-ray spectrum cannot be produced by hot electron bremsstrahlung alone. A large gamma-ray excess > 8 MeV above the hot electron bremsstrahlung spectrum must be present in order to produce the observed e+e- spectra and photo-neutron yields. These results are independent of, but fully support, the gamma-ray HEB detected by the SAS.

4. DISCUSSIONS

If the TPW gamma-ray excess > 8 MeV is not emitted by hot electron bremsstrahlung, then what could be emitting the HEB? While we are pursuing different theoretical models, at this point one tantalizing candidate is Compton up-scattering of focal-spot keV x-rays by the hot electrons. This hypothesis is motivated by two facts: (a) the HEB is absent in directions far from laser forward; (b) the HEB peak is close to the observed hot electron energy peak. Below is a brief discussion of the order-of-magnitude considerations for a Compton upscattering origin of the HEB.

We first review the TPW laser parameters: The "50% energy focal-spot" radius of TPW is ~ 3 microns. The average on-target TPW energy is ~ 130 J. Hence the average focal-spot laser fluence is $F = 65 \text{ J}/\pi(3 \cdot 10^{-4} \text{ cm})^2 = 2.3 \cdot 10^8 \text{ J/cm}^2$. When a relativistic electron of Lorentz factor $\gamma \gg 1$ hits a soft photon of energy ϵ_0 in the laboratory frame, the Compton formula from standard textbooks (e.g. Rybicki and Lightman 1979) gives the Compton upscattered photon energy in the forward direction as $\epsilon_{sc} = 4\gamma^2\epsilon_0$. The factor γ^2 comes from performing the Lorentz transformation twice, from the lab. frame to the electron rest frame, and then back to the lab. frame after performing the scattering in the electron rest frame.

Most observed hot electrons and gamma-ray bumps for Pt targets peak around ~ 17 MeV. Hence $\gamma \sim 34$ and $\epsilon_{sc} \sim 17$ MeV. From the Compton formula above we find that the characteristic x-ray energy ϵ_0 needed for Compton scattering to produce the observed gamma-ray peak is $\epsilon_0 = 17 \text{ MeV}/(4\gamma^2) = 3.6 \text{ keV}$. Let us assume that a fraction f of incident laser fluence F is somehow converted into multi-keV x-rays near the focal spot. The corresponding x-ray number fluence is $N_x = fF/\epsilon_0 = f \cdot 2.3 \cdot 10^8 \text{ J/cm}^2 / (3.6 \text{ keV} \cdot 1.6 \cdot 10^{-16} \text{ J/keV}) = f \cdot 4 \cdot 10^{23} \text{ x-rays/cm}^2$. In our case, Compton scattering occurs in the Thomson regime (instead of the Klein-Nishina regime, Rybicki & Lightman 1979) since $\gamma \epsilon_0 < mc^2$. Hence we can use the Thomson cross-section $\sigma_T = 6.7 \cdot 10^{-25} \text{ cm}^2$ to calculate the total scattering probability of each hot electron against the "column density" of x-rays: $P_{scatt} = \sigma_T \cdot N_x = (6.7 \cdot 10^{-25} \cdot f \cdot 4 \cdot 10^{23}) = 0.27f$. Despite the small Thomson cross-section, this theoretical scattering probability is not negligible for TPW parameters. Note that each hot electron transfers its entire energy to a gamma-ray in a single scattering due to its large γ as long as it can find a x-ray of the right energy to scatter. Hence Compton scattering is much more efficient than bremsstrahlung in its radiation efficiency. We note also that P_{scatt} scales linearly with laser energy and scales with γ^2 which is proportional to laser intensity. Hence a laser with lower energy add lower intensity than TPW will likely have negligible P_{scatt} . This may explain why other "weaker" short-pulse lasers cannot produce any measurable gamma-ray bump.

Next, let us see what kind of fraction f we need in order to achieve the observed gamma-ray "bump" of Fig. 1a. Averaging over all of our data sets, we obtain average (> 8 MeV) gamma-ray energy in the HEB $\sim 2 - 4$ J, while the deduced hot electron energy averages $\sim 20 - 40$ J. Hence the average conversion efficiency of hot electron energy to HEB gamma-rays > 8 MeV is ~ 0.1 . In the context of the Compton upscattering scenario, this implies $P_{\text{scatt}} \sim 0.1$. Comparing this to the theoretical scattering probability of $0.27f$ above, we find $f \sim 0.37$. In other words, we may need to convert $\sim 1/3$ of focal-spot laser fluence into multi-keV x-rays, in conjunction with hot electron acceleration, in order to produce the observed HEB gamma-rays via Compton upscattering of focal-spot x-rays. The fact that f is not off by many orders of magnitude motivate us to further pursue the Compton scattering scenario. The next step is to perform detailed radiation-hydro simulations of laser absorption to emit the x-rays and particle-in-cell simulations of hot electron acceleration. We plan to use the FLASH code for the first task and the EPOCH code for the second task. Both the x-ray and hot electron spatial and temporal profiles will be used in a combined GEANT4 simulation.

ACKNOWLEDGEMENTS

At Rice University this work was supported by DOE grant DE-SC0021327. At UT Austin, his work was supported by the DOE, Office of Science, Fusion Energy Sciences under Contract No. DE-SC0021125: LaserNetUS: A Proposal to Advance North America's First High Intensity Laser Research Network".

Table 1. TPW laser parameters of our 2022 60-shot run

	Energy	Pulse Duration (fs)	Peak Power (TW)	closed Radius with 50%	Peak Intensity (W/cm ²)	Strehl
AVERAGE	123.25	161.05	781.82	3.8	2.96E+21	0.68
MEDIAN	122.57	158	794.12	3.72	2.89E+21	0.7
MIN	104.2	128	531.29	2.42	1.85E+21	0.46
MAX	139.18	216	1060.68	5.39	4.68E+21	0.82

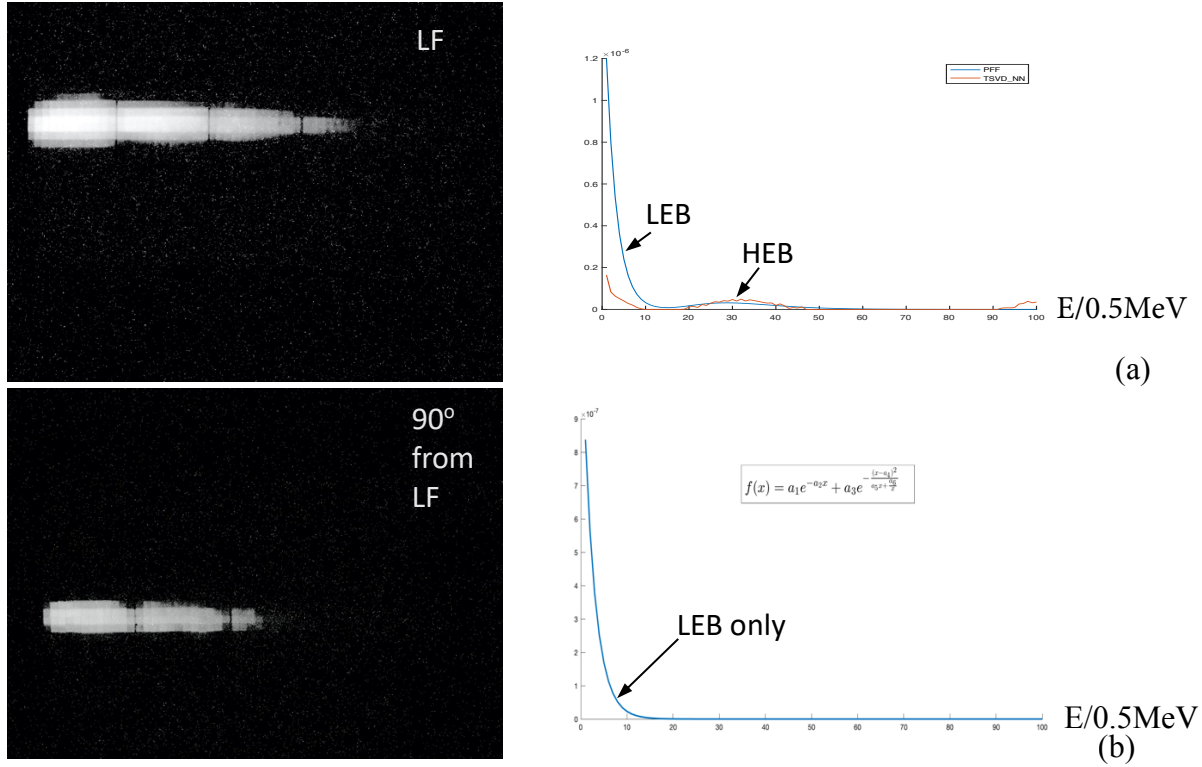


Fig.1 (a) Sample raw SAS image (left) and inverted gamma-ray spectrum (right) obtained at laser forward (LF) from our 2022 TPW experiment. TSVDNN denotes the model-independent spectrum directly inverted from the image. PFF denotes the best-fit analytic spectrum derived from the TSVDNN solution. Both spectra show two distinct spectral components. LEB denotes the low-energy bremsstrahlung component below 8 MeV and HEB denotes the broad high-energy bump above 8 MeV. See Liang et al 2022 for discussions of our inversion algorithm; (b) sample SAS image (left) and inverted spectrum (right) obtained at 90° from LF. Here the best-fit spectrum shows no HEB component. The x-axes of both spectra are in units of 0.5 MeV. The y-axes units are arbitrary. Almost all SAS spectra obtained at LF and 90° from LF resemble these two examples.

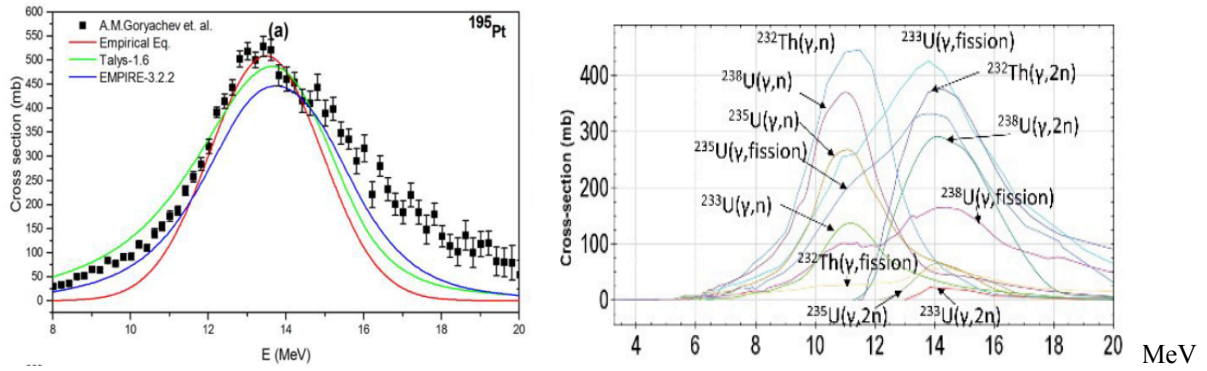


Fig.2 (left); (γ, n) photo-neutron reaction cross-section of Pt shows the GDR peak at ~ 13.5 MeV (from Makwana et al 2017); (right) (γ, Nn) and $(\gamma, \text{fission})$ reaction cross-sections of Th and U isotopes show GDR peaks between 11 and 16 MeV (from Kimura et al 2016). All GDR peaks of high-Z elements extend from ~ 8 MeV to ~ 20 MeV, which coincide with the HEB gamma-rays > 8 MeV of Fig.1. The LEB component of Fig.1 contains very few gamma-rays at GDR energies compared to the HEB.

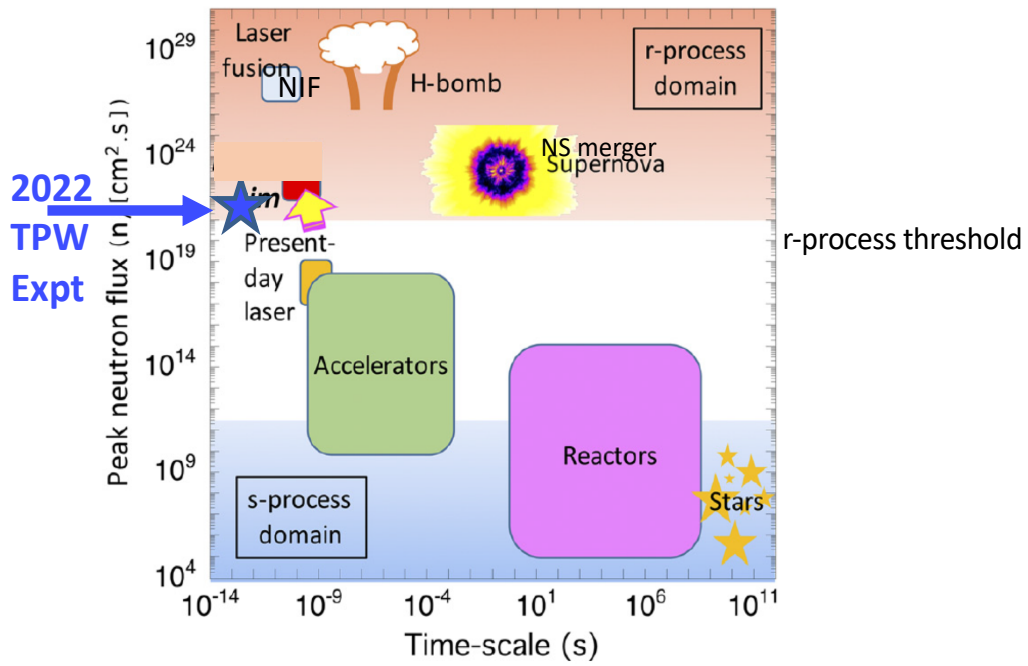


Fig.3 Comparison of peak neutron flux achieved in our 2022 TPW experiment with other man-made and cosmic neutron fluxes relevant to r-process element creation (figure adapted from Chen et al 2019).

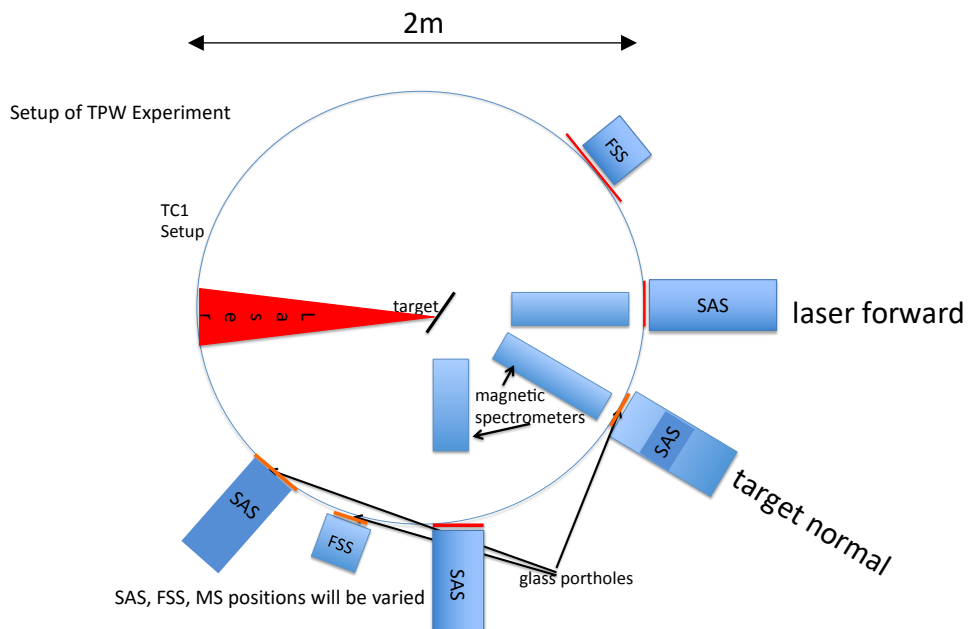
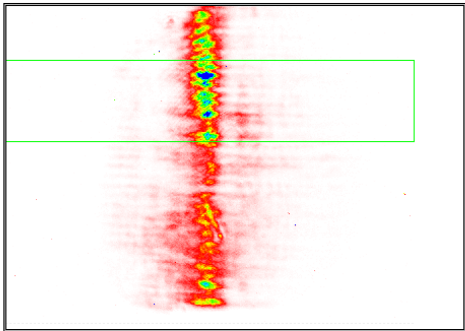
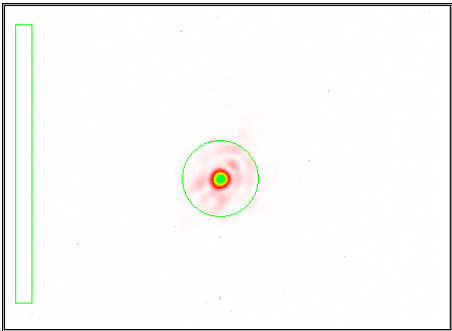


Fig.4 Typical diagnostics set-up in TC1 of TPW. Not shown are the gamma dosimeters and neutron bubble detectors attached to the outside of the tank wall. To minimize attenuation most FSS's and SAS's view the target through aluminum windows. In 2022 the laser incidence angle was 17° . The target orientation was s-polarized.

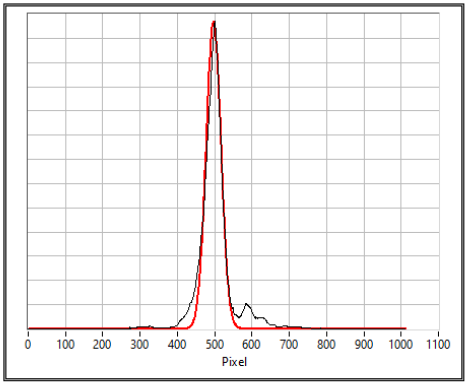
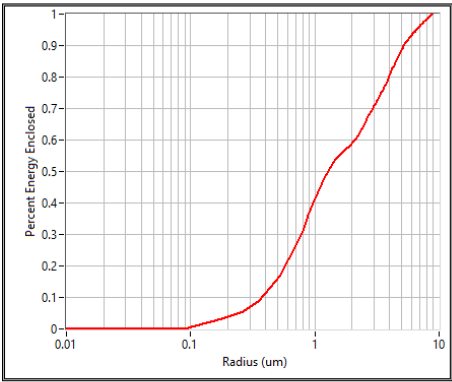
SHOT# 014897 2022-06-23



Energy
135 J

Pulse Duration
138 fs

Power
980 TW



(b)

6/23/2022 4:22:12 PM

Fig.5 Sample laser pulse spatial and temporal profiles of a TPW shot during our 2022 run. The peak intensity was $4.7 \times 10^{21} \text{W.cm}^{-2}$ for this shot.

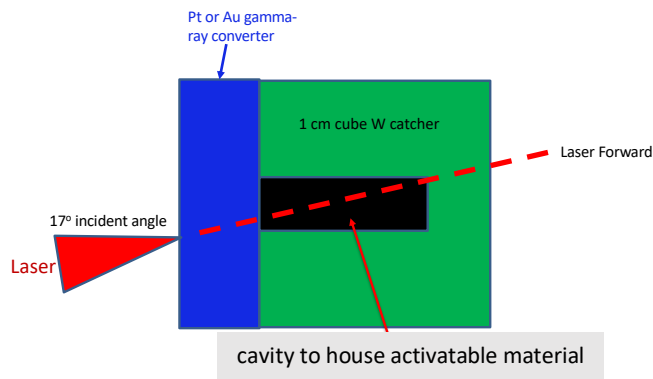


Fig.6 Sketch of capsule target design to fully contain and shield any potentially radioactive products from post-shot targets for safe and easy handling. The capsule consists of a 1 cm cube of W catcher with a cylindrical divot or cavity to house any activatable material. The Pt or Au gamma-ray converter serves as a removable capsule cover. This design worked well in our 2022 experiment. The laser aiming position on the front surface varies with converter thickness such that the forward gamma-ray cone covers the desired volume of the cavity. Due to the width of the gamma-ray cone we can shoot the same target multiple times by simply shifting the target position by a small amount, depending on the crater size of the previous shot. In 2022, we managed to shoot the same target up to 5 times. All data reported in this paper came from flat disks and empty capsules only.

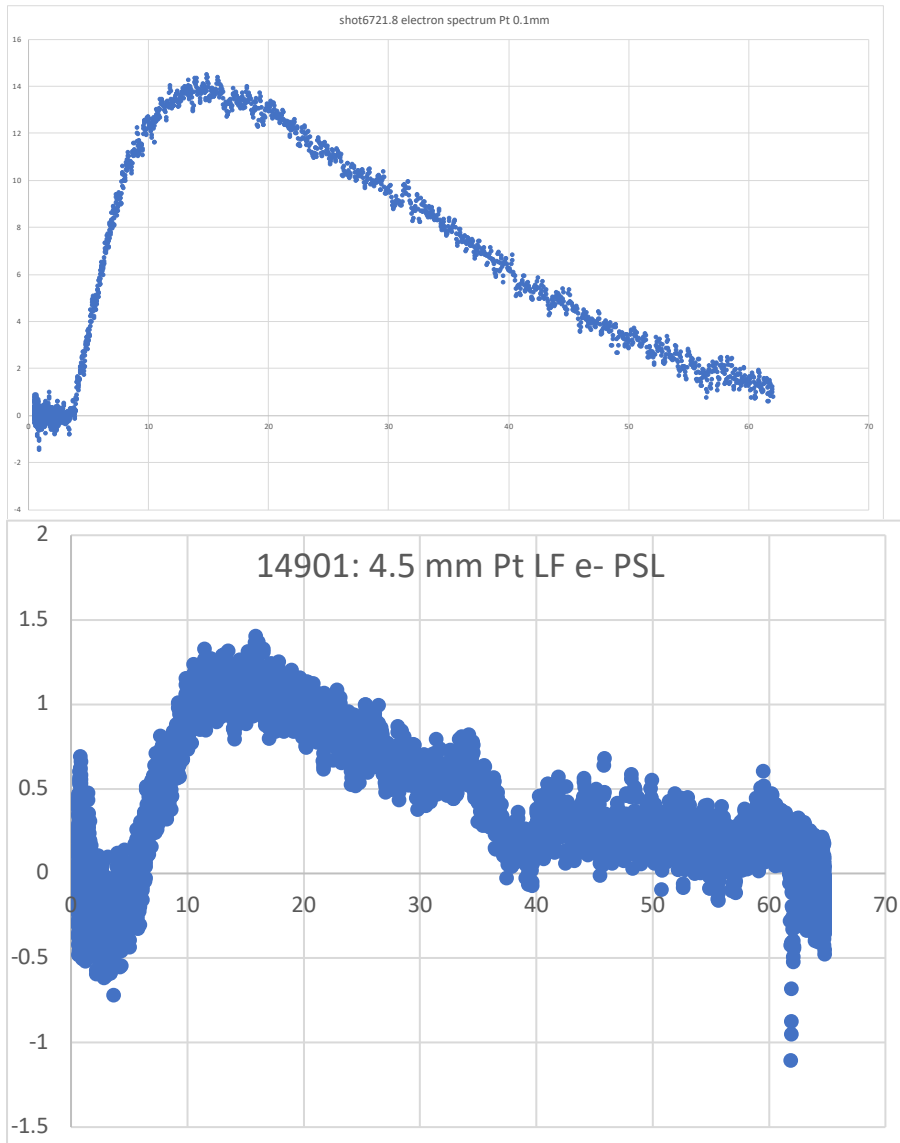


Fig.7 Sample measured hot electron spectra from a 0.1 mm thick Pt target (top) and a 4.5 mm thick Pt target (bottom) show similar spectral shapes despite a factor of 45 difference in target thickness. The relative stability of the hot electron spectral shape and peak energy vs. target thickness allows us to confidently use this spectral shape for hot electron injection in GEANT4 simulations. We scale the electron injection number to match the predicted emergent outputs in e^+e^- pairs, gamma-rays and neutrons with experimental data, and then check for consistency among the different data sets.

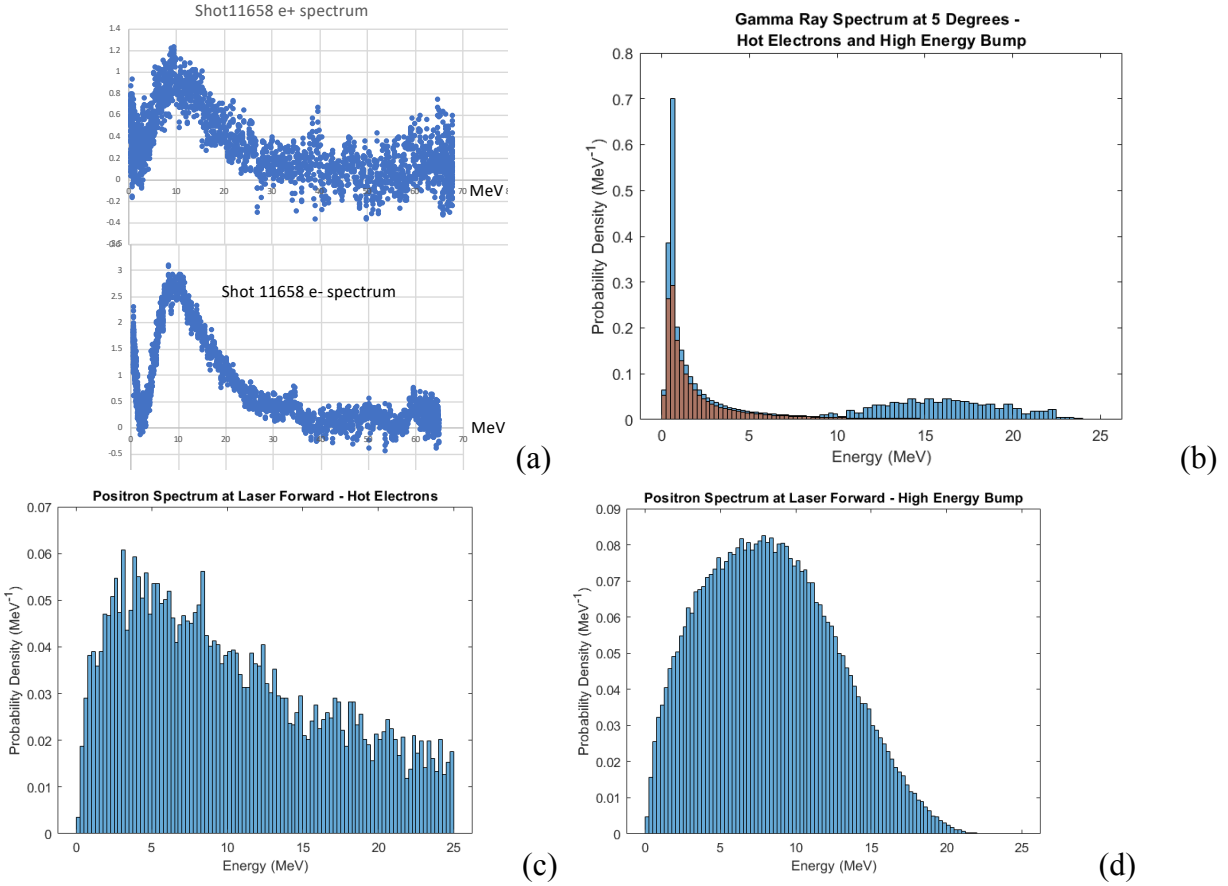


Fig. 8 (a) Observed electron and positron spectra for a thick Pt target show almost identical shapes, peak energies and amplitude, showing that both are created by the same gamma-rays with no sheath field effects. The positron spectrum peaks at $\sim 8-9$ MeV. All primary hot electrons are absorbed in such thick targets except for the high energy tail above 30 MeV. (b) GEANT4-predicted gamma-rays from two different injection models: brown curve: only hot electrons of Fig.7 spectrum without additional gamma-rays from the HEB of Fig.1; blue curve: hot electrons plus HEB gamma-rays of Fig. 1, (c) predicted positron spectrum from pure hot electron injection without the HEB gamma-rays disagrees with the positron spectrum observed in Fig.8(a). The positrons created by bremsstrahlung gamma-rays peak at $\sim 2-3$ MeV. (d) predicted positron spectrum from injection of hot electrons plus HEB gamma-rays peak at ~ 8 MeV, which roughly agrees with the observed positron spectrum in Fig.8(a).

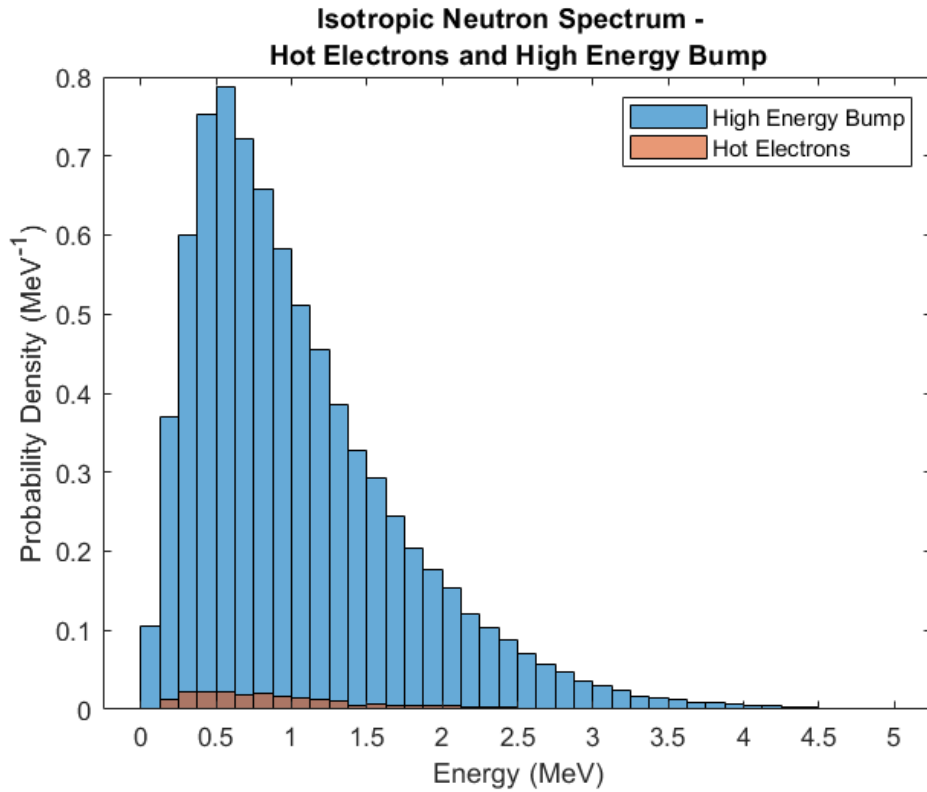


Fig.9 GEANT4-predicted emergent neutron spectra from the two types of injection models used in Fig.8(b): brown curve: hot electrons only without HEB gamma-rays of Fig.1a; blue curve: hot electrons plus HEB gamma-rays of Fig.1a. The predicted neutron number of the blue curve agrees with bubble detector data to within ~ 20%, whereas the predicted neutron number of the brown curve is ~ 30 times lower than observed.

References

- K. T. Behm, J et al., 2018, Rev. Sci. Instrum 89, 113303.
- Chen, C.D. et al., 2009, Phys. Plasmas 16, 082705.
- Chen, H. et al. 2009, Relativistic positron creation using ultraintense short pulse lasers. Phys. Rev. Lett. 102, 105001.
- Chen, S.N. et al 2019, "Extreme brightness laser-based neutron pulses as a pathway for investigating nucleosynthesis in the laboratory", Matter Radiat. Extremes 4, 054402 (2019); doi: 10.1063/1.5081666.
- Gibbon, P. 2005, "Short Pulse Laser Interactions with Matter" (Imperial College Press, UK).
- Goriely, S. and Pinedo, G.M. 2015, The production of transuranium elements by the r-process nucleosynthesis, Nuclear Physics A944 158–176.
- Gunther, M.M. et al. 2022, "Forward-looking insights in laser-generated ultraintense γ -ray and neutron sources for nuclear application and science", Nat. Comm. 13:170 | <https://doi.org/10.1038/s41467-021-27694-7> | www.nature.com/naturecommunications.
- Henderson, A. 2015, "Monte-Carlo Simulation and Measurements of Electrons, Positrons, and Gamma-rays Generated by Laser-Solid Interactions", Rice University PhD Thesis.
- Henderson, A., et al. 2014, "Ultra-intense Gamma-Rays Created using the Texas Petawatt Laser," High Energy Density Physics, 12, 46.
- Kajimo, T. et al 2019, "Current Status of r-Process Nucleosynthesis", Progress in Particle and Nuclear Physics C, 107, 109.
- Kimura, R. et al 2016, "Principle validation of nuclear fuel material isotopic composition measurement method based on photofission reactions", J. of Nucl. Sci. and Tech. 53, 1177471.
- Kojima, S. et al 2014, Plasma Fusion Res 9, 4405109.
- Leemans, W.P., 2001, Phys. Plasmas 8, 2510.
- Levy, M. et al. 2014, Petawatt Laser Absorption Bound. Nature Comm. 5, 4149.
- Liang, E., Wilks, S. & Tabak, M. 1998, Pair production by ultraintense lasers. Phys. Rev. Lett. 81, 4887.
- Liang, E. et al 2015, "High e^+/e^- Ratio Dense Pair Creation with 10^{21}W.cm^{-2} Laser Irradiating Solid Targets" Scientific Reports, 5:13968| DOI: 10.1038/srep13968, available on www.nature.com/scientificreports/
- Liang, E. et al 2022, "A scintillator attenuation spectrometer for intense gamma-rays", Rev. Sci. Instr. 93, 063103.
- Makwana, R. et al 2017, "New Empirical Formula for (gamma, n) Reaction Cross Sections near to GDR Peak for Elements with $Z \geq 60$ ", Chinese Phys. C 41, 044105.
- Martinez, M. et al. 2005, The Texas Petawatt Laser. Proc. of SPIE, 5991(59911N-1).
- Morgan, G.L. et al., 1991, Nucl. Instrum. Methods Phys. Res., Sect. A 308, 544 (1991).
- Naik, H. et al 2011, "Mass Distribution in Bremsstrahlung-induced Fission of ^{232}Th , ^{238}U and ^{240}Pu ", Nuclear Phys. A 853 2011.
- Pomme, S. 1994, "Fragment Characteristics for the Photofission of ^{238}U with 61-13.1 MeV Bremsstrahlung", Nucl. Phys. A 572, 237.
- Rybicki, G. and Lightman, A. 1979, "Radiativ Processes in Astrophysics" (Wiley, NY).
- Tanaka, K.A. et al 2019, "Current status and highlights of the ELI-NP research program", Matter Radiat. Extremes 5, 024402 (2020); doi: 10.1063/1.5093535.